

## Thermodynamic Structure of the Solar Corona: Tomographic Reconstructions and MHD Modeling

Diego G. Lloveras<sup>1</sup>  · Alberto  
M. Vásquez<sup>1,2</sup>  · Federico A. Nuevo<sup>1,3</sup>  ·  
Cecilia Mac Cormack<sup>1,2</sup>  ·  
Nishtha Sachdeva<sup>4</sup>  · Ward Manchester  
IV<sup>4</sup>  · Bartholomeus Van der Holst<sup>4</sup>  ·  
Richard A. Frazin<sup>4</sup> 

© Springer ....

**Abstract** Observational techniques play an essential role in advancing our understanding of the physics of the solar corona. They provide validation data

- 
- ✉ D.G. Lloveras  
dlloveras@iafe.uba.ar
  - ✉ A.M. Vásquez  
albert@iafe.uba.ar
  - ✉ F.A. Nuevo  
federico@iafe.uba.ar
  - ✉ C. Mac Cormack  
cmaccormack@iafe.uba.ar
  - ✉ N. Sachdeva  
nishthas@umich.edu
  - ✉ W. Manchester IV  
chipm@umich.edu
  - ✉ B. Van der Holst  
bartvand@umich.edu
  - ✉ R.A. Frazin  
rfrazin@umich.edu

<sup>1</sup> Instituto de Astronomía y Física del Espacio (IAFE), CONICET-UBA, CC 67 - Suc 28, (C1428ZAA) Ciudad Autónoma de Buenos Aires, Argentina

<sup>2</sup> Universidad Nacional de Tres de Febrero (UNTREF), Valentín Gómez 4752, (B1678ABH) Caseros, Provincia de Buenos Aires, Argentina

<sup>3</sup> Ciclo Básico Común (CBC), Universidad de Buenos Aires (UBA), Buenos Aires, Argentina

<sup>4</sup> Department of Climate and Space Sciences and Engineering (CLaSP), University of Michigan, 2455 Hayward Street, Ann Arbor, MI 48109-2143, USA

for three-dimensional (3D) magnetohydrodynamic (MHD) models of the solar atmosphere, key to improve their space weather forecasting capabilities. Solar rotational tomography (SRT) is currently the sole observational technique that provides an empirical 3D description of some of the fundamental plasma parameters of the solar corona at a global scale. Based on EUV data of space borne instruments, SRT allows constructing 3D maps of the coronal electron density and temperature at heliocentric heights below 1.25 R<sub>sun</sub>. We carry out a study of the corona combining tomographic reconstructions with MHD simulations using the latest version of the Alfvén Wave Solar Model (AWSoM) of the Space Weather Modeling Framework (SWMF). Target rotations were selected from the solar minimum between solar cycles (SC) 23 and 24 and the current declining phase of solar cycle 24. Tomographic reconstructions and results of the model are analyzed in distinct coronal magnetic structures. We study magnetically closed structures associated with the equatorial streamer belt, as well as magnetically open regions enclosing it. We report on the tomographic results in the different structures, their implications for the physics of the solar corona, and the current capability of the AWSoM model to reproduce the tomographic reconstructions in different regions.

**Keywords:** Solar Cycle, Observations; Corona,E; Corona, Structures

## 1. Introduction

Being the place where the solar atmosphere is heated and the solar wind accelerated, and where impulsive events such as solar flares and coronal mass ejections are energized, observation and modeling of the solar corona are tasks of great relevance to improve our understanding of the Sun-Earth environment. To advance our knowledge of the physics of the solar corona, as well as to improve its three-dimensional (3D) models, information derived from observational data plays a key role. Solar rotational tomography is currently the sole observational technique able to provide a quantitative empirical description of the 3D distribution of some fundamental plasma parameters of the solar corona at a global scale.

NOTE: Here we will put in a couple of paragraphs summarizing what SRT and DENT are, including references and defining the accronyms in the process. We should refer to minima in particular. We should mention the instruments and missions we use as data for DENT, and define their accronyms too. Also, a couple of paragraphs on the AWSoM model and the SWMF, including references and defining the accronyms in the process.

## 2. Methodology

### 2.1. DENT reconstructions

NOTE: This section will summarize DENT's main aspects and equations, only those needed to understand the paper. Nothing not needed to read this paper is

---

provided. Also, no derivation of equations are provided. References are given so that the reader can dig deeper if so desires. Points to cover are:

- Selected targets, instruments used. One paragraph.
- Characteristics of the data (specific time series, dates, bands, etc.), SolarSoft software version used for their processing. One paragraph.
- Technical aspects of DENT (grid, regularization, off-limb data is only used) and how these differ from previous versions (rereferences). One paragraph.
- What is FBE, what is LDEM, what is R. Why we care about these three quantities and what is their physical meaning should be clear. Then the final products  $N_m$  and  $T_m$ , and what is their physical meaning.

$$\text{FBE}_i^{(k)} = \int dT \text{LDEM}_i(T) \text{TRF}^{(k)}(T), \quad k = 1, \dots, K \quad (1)$$

Due to unresolved coronal dynamics, tomographic reconstructions exhibit negative values of the reconstructed FBE, or zero when the solution is constrained to positive values (Frazin, 2000; Frazin, Vásquez, and Kamalabadi, 2009). These non-reconstructed voxels are indicated as black voxels in the Carington maps of the reconstructed DENT results in Section 3.

Once the LDEM is determined at each voxel, the average squared electron density  $\langle N_e^2 \rangle$  and the electron mean temperature  $T_m$  in the voxel can be computed by taking its zeroth and first moments over temperature. More specifically, at the  $i$ -th voxel,

$$N_{m,i}^2 = \langle N_e^2 \rangle_i = \int dT \text{LDEM}_i(T), \quad (2)$$

$$T_{m,i} = \langle T_e \rangle_i = \frac{1}{\langle N_e^2 \rangle_i} \int dT T \text{LDEM}_i(T), \quad (3)$$

We define next a measure of the average relative difference between the tomographic and the synthetic FBE in each voxel, as

$$R_i \equiv (1/K) \sum_{k=1}^K \left| 1 - \text{FBE}_{i,\text{syn}}^{(k)} / \text{FBE}_{i,\text{tom}}^{(k)} \right|, \quad (4)$$

so that the final product of DENT is in the form of 3D maps of the electron density and mean temperature. These relationships were derived in detail in Frazin, Vásquez, and Kamalabadi 2009 (see Appendix C).

Aclarar que consideramos  $N_e$  como  $\sqrt{\langle N_e^2 \rangle}$ . ALBERT: Yo creo que es mejor hablar de  $\sqrt{N_m^2}$

DENT has been improved since the previously published work. We now perform hollow-tomography with the EUV images, (definir hollow-tom) and a 3D regularized of the solution was applied to obtain smother and more reliable result at the edge of the tomographic grid. **NOTA de Albert: Explicá que hacés**

sin justificarte. Luego aclará como se hizo eso en trabajos previos, y cual es el impacto esperado. Puedo proveer un párrafo de ejemplo, pero creo que será mejor que vos escribas como te salga y yo luego edito. Algo muy importante para todo el paper: proponete escribir “párrafos modulares”. Es decir que, con las razonables limitaciones, puedan moverse de lugar, de orden, y sigan funcionando. No definiría hollow-tomography, es un término coloquial interno nuestro. Lo correcto es que al hablar de datos mucho más arribas expliques que los datos del disco no se utilizan, pero no le des un nombre a la tomografía.

## 2.2. AWSoM simulations

NOTE: This section will summarize the AWSoM model. After a first version is written we will surely require some input from the Michigan friends. Points to cover:

- Data input. Link with the data input for DMT in terms of dates, etc. One paragraph.
- Main physical and technical aspects (grid in particular) of the model. One paragraph.
- Explain the artificially extended TR. One paragraph.
- What are the products of the model we care about in this paper. One paragraph.

In the transition region (TR), the plasma heats up and becomes less dense by several orders of magnitude over a short distance. Modeling this region realistically has a very high computational cost. For this reason, the model uses an artificially extended TR about  $\approx 0.05 R_{\odot}$  thick, as well as artificially large values for the electronic density and temperature as boundary conditions in  $r = 1 R_{\odot}$ . Consequently, model results below  $\approx 1.05 R_{\odot}$  were not taken into account in this article.

## 2.3. Tracing of results along fieldlines

NOTE: This section will explain how the AWSoM magnetic model is used to trace the thermodynamic products of both DMT and AWSoM along the fieldlines of AWSoM. This requires covering the following points:

- A first paragraph qualitatively describing the process. This includes mentioning that the AWSoM products are first interpolated into the DMT grid.
- A short paragraph describing the numerical method used to trace field lines. We have a nice version of this in your previous paper. At this point the reader should understand that for each field line we have its geometry  $\mathbf{r}(s)$  as a function of the distance  $s$  along the loop, with  $s(1 R_{\odot}) \equiv 0$ .
- Explain very simply how then that for each voxel the middle point of the field line is selected and assigned the DMT and AWSoM products of that cell. At this point the reader should understand that for each field line we have:  $Q[r(s)]$ , where  $Q$  is any given quantity from either the DMT model (specifically  $\sqrt{N_m^2}$  and  $T_m$ ) or the AWSoM model (specifically  $N_e$  and  $T_e$ ).

- 
- Explain fits to the DEXT results  $\sqrt{N_m^2}(r)$ ,  $T_m(r)$ .
  - Explain then the classification of field lines.

For both rotations, the DEXT and AWSOM 3D maps of electron density  $N_e$ , electron mean temperature  $T_m$  and electron temperature  $T_e$  respectively were traced along the magnetic field lines modeled using AWSOM as described at the end of Section 2.1. In the case of closed loops, results were separated into their two legs, defined as the two segments that go from the coronal base up to the apex.

For each open field line, and for each leg of the closed ones, an exponential fit was then applied to the  $\sqrt{N_m^2}(r)$  data points, and a linear fit applied to the  $T_m(r)$  data points, as described by

$$\sqrt{N_m^2} = N_0 \exp[-(h/\lambda_N) / (r/R_\odot)] \quad (5)$$

$$T_m = T_0 + m h \quad (6)$$

where  $h \equiv r - 1 R_\odot$  is the coronal height measured from the photosphere. In the electron density fit,  $\lambda_N [R_\odot]$  is the density scale height and  $N_0 [\text{cm}^{-3}]$  is the electron density at the footpoint ( $h = 0$ ) of the loop. In the electron temperature fit,  $m [\text{MK}/R_\odot]$  is the slope and  $T_0 [\text{MK}]$  is the electron temperature at the footpoint of the loop. The slope  $m$  is the radial gradient of the electron temperature along the loop, which we denote as  $m = \nabla_r T_m$  hereafter, being  $\nabla_r \equiv \mathbf{e}_r \cdot \nabla$  the radial derivative operator, where  $\mathbf{e}_r$  is the heliocentric radial unit vector.

In the case of the electron density, the fitted function corresponds to the isothermal hydrostatic equilibrium solution, allowing for variation of the solar gravitational acceleration with height. This choice of function provides a straightforward means to directly evaluate how compatible is the observed coronal thermodynamical state with the hydrostatic solution.

In the present work we focus on lines with increasing and decreasing temperatures in linear form. In other words, we selected those legs where the Pearson correlation coefficient  $\rho$  between temperature  $T$  and radius  $r$  meets  $|\rho(T, r)| > 0.5$ . (with p-value less than 0.05). In this way, those legs in which the DEXT results cannot ensure a noticeable change in temperature between the base and the apex, are discarded.

The linear fit allows characterization of its variation with height by means of a characteristic temperature gradient  $\nabla_r T_m [\text{MK}/R_\odot]$  along each leg. **En realidad esta regresion lineal utiliza de por si los errores, pero luego tmb los uso para el test de hipotesis, quizas vale la pena ponerlo solo ahi.**

To measure how good the quality of the exponential fit to the electron density and the linear fit to the temperature data are, a chi-square merit function was used (see Section 15.2 Press *et al.* (2002)). The errors were estimated in Lloveras *et al.* (2017), 0.07 MK for  $T_m$  and  $4.0 \cdot 10^6 \text{cm}^{-3}$  for  $N_e$  and legs with p-value  $> 0.005$  were rejected.

To be selected a leg must meet all following conditions.

- The leg must go through at least five tomographic grid cells with reconstructed data, and there must be at least one data point in each third of the range of heights spanned by the leg.

- ii) The value of the Pearson correlation coefficient meets  $|\rho(T, r)| > 0.5$ .
- iii) The p-value of both the exponential and linear fit must be less than 0.05.

For the two targeted rotations, DENT and AWSOM results were traced along the AWSOM field lines, which provides a way to characterize the global thermodynamic state of the inner solar corona and to compare them. To that end four different types of legs corresponding with four different types of magnetic structures were selected:

- Type 0 - Small (meaning with apex within the DENT range of heights) closed field lines in the latitudes range  $[-30^\circ, +30^\circ]$  and  $\nabla_r T_m < 0$ .
- Type I - Small closed field lines in all latitudes, with  $\nabla_r T_m > 0$ .
- Type II - Large closed field lines (meaning their apex surpasses the DENT range of heights) in the latitudes range  $[-90^\circ, -30^\circ] \cup [+30^\circ, +90^\circ]$  and  $\nabla_r T_m > 0$ .
- Type III - Open field lines (meaning with apex out the DENT range of heights) in the latitudes range  $[-90^\circ, -60^\circ] \cup [+60^\circ, +90^\circ]$  and  $\nabla_r T_m > 0$ .

Hice las definiciones con gradiente de temperatura para que quede mas claro, pero en realidad uso el pearson. NOTE: Charlemos los tres en persona de esto.

#### 2.4. Energy input flux

NOTE: This section will summarize how loop integrated energy quantities are computed from the DENT products and the AWSOM magnetic model alone. The summary will not include any derivation and will refer to Cecilia's paper. Only the results that are relevant are to be explicated. Start by explaining the model and assumptions, and end up summarizing the loop-integrated products (radiative and conductive fluxes). At the end the reader should understand that their sum is the energy input flux required at the coronal base to maintain the loop stable. This should be a very short section, as it is a summary of one previous paper alone.

Due the difference between temperatures of transition region and solar corona, there must to be a heating mechanism that compensate all the losses present in the atmosphere and maintain stable the plasma temperature. Previous works have studied this mechanism by observations and modeling, but mostly for active regions. Mac Cormack *et al.* (2017) have developed a technique that estimate the heating injected into the loops during a period of minima activity. Using DENT combined with an extrapolation of magnetic field, as we detailed before, they obtain the different plasma parameters along each magnetic loop, and therefore, compute the energy input flux required to maintain them stable. The model assume a simple energy balance for each magnetic flux tube, where the losses by radiative power ( $E_r$ ) and thermal conduction power ( $E_c$ ) are compensated by some coronal heating power( $E_h$ ) (Aschwanden, 2004):

$$E_h(s) = E_r(s) + E_c(s), \quad (7)$$

---

where  $s$  is the position along each magnetic flux tube and the powers are in units of  $[\text{erg sec}^{-1} \text{cm}^{-3}]$ .

Thermal conduction power is calculated by the Spitzer model (Spitzer, 1962), which describes coronal plasma regime properly. The thermal conduction power is obtained by taking the divergence of the conductive loss function  $F_c(s) = -\kappa_0 T(s)^{5/2} \frac{dT}{ds}(s)$ , where  $\kappa_0 = 9.2 \times 10^{-7} \text{erg sec}^{-1} \text{K}^{-7/2}$  is the Spitzer thermal conductivity. Due in coronal regime, the plasma is confined to the magnetic field, thus conduction is also predominately in the magnetic field direction. Thus, divergence is only the derivative along the position  $s$ :

$$E_c(s) = \frac{1}{A(s)} \frac{d}{ds} [A(s) F_c(s)]. \quad (8)$$

where  $A(s)$  represent the magnetic flux tube area along the position  $s$ .

Radiative power depends on the amount of plasma in certain temperatures that can radiate. The model estimate it by integrating the squared density multiplied by a radiative loss function  $\Lambda(T)$ . This function depends on plasma temperature and is calculated by the atomic database and the plasma emission model from CHIANTI (Del Zanna *et al.*, 2015). Then, the expression for radiative power obtained is:

$$E_r = \int dT T \text{LDEM}(T) \Lambda(T) \quad (9)$$

Taking into account the null divergence condition of magnetic field, the model integrate, between tomographic limits, each power quantities over magnetic flux tube independently of its area. Therefore, a loop-integrated equation for the energy flux balance is obtained ( $[\text{erg sec}^{-1} \text{cm}^{-2}]$ ):

$$\phi_h = \phi_r + \phi_c. \quad (10)$$

where  $\phi_{h,r,c}$  are the loop-integrated energy input flux, radiative flux and conductive flux for each magnetic field line at  $1.025 R_\odot$ .

For a complete description of the energy balance model, the reader can refer to Mac Cormack *et al.* (2017). We compute the loop-integrated energy quantities for both rotation analyzed in this work.

### 3. Results

#### 3.1. Tomographic Results

NOTE: This section will show first the DGMT products in the form of Carrington maps at three heights, for the two target rotations. It will then show the latitude/longitude location of the four types of magnetic loops (defined in Section 2.3) at a sample height. Then, for the each type of loop, we will show histograms

of the values of different DENT products traced along them, characterizing in a quantitative fashion the DENT results in distinct magnetic structures. It will also include a quantitative comparison between the two target rotations of the median values of the DENT products in each type of loop.

To perform a comparative study of the thermodynamic structure of the inner corona in different solar cycles we carry out a DENT reconstruction for two rotations: CR-2082, using STEREO/EUVI data and CR-2208, using SDO/AIA data. Once the LDEM was determined for each rotation, the square root of the mean value of the electron density squared  $\sqrt{N_m^2}$  and the electron mean temperature  $T_m$  were computed at each voxel of the tomographic computational grid by means of Equations 2 and 3. As an example, Figures 1 and 2 show the latitude-longitude maps of DENT results for both rotations at three different heights of interest. The lowest height where the tomography gives results, the lowest height where the AWSOM model results are reliable and a representative average height were selected, that is  $r = 1.025, 1.065$  and  $1.105, R_\odot$  respectively. Black voxels correspond to non-reconstructed voxels (explained in Section 2.1). Thick-black curve indicates the magnetic open/closed boundary based on the magnetic field of AWSOM model.

While CR-2082 was highly axisymmetric and showed virtually no ARs (active region) (ver si en lat 50 y long 70 hay una.), CR-2208 showed an AR around latitude  $+10^\circ$  and longitude  $300^\circ$  (ver la region open en lat 0 y long 200). Except for these ARs, in both rotations the open-closed boundaries derived from the respective AWSOM model match the shape of the contour levels of the tomographic maps of both the electron density and the electron mean temperature. In the AR, there is a lack of match between the open-closed boundaries and the tomographic reconstructions of density and temperature, that is why those ranges were excluded from the analysis.

PARRAFO CORTO DE OBSERVACIONES QUE LUEGO SERAN CORROBORADAS CON HISTOGRAMAS. A visual inspection of Figures 2 and 3 suggest/indicates that the streamer region of CR-2082 was denser and colder than CR-2208. In both rotations, but specifically in CR-2082 the temperature in the equatorial latitudes tend to decrease with height while the latitudes between the open-close boundaries and the equatorial latitudes tend to increase. These thermodynamic structures have been reported for other rotations in previous works (Lloveras *et al.*, 2017). Closed regions are characterized by relatively larger values of density and temperature in comparison to the open regions. **que mas se puede agregar?**

To study the variation of the DENT results in different magnetic structures we traced  $\sqrt{N_m^2}$  and  $T_m$  along the magnetic field lines of the AWSOM model. For both rotations, all field lines that meet the criteria listed in Section 2.3 were selected. For each field line, the data points of electron density and electron mean temperature as a function of height were fitted to the Equations 5 and 6.

aca se definen los highpoints, se comentan los colores y enunciar que cada uno puebla una region termodinamica diferente

As a result, the electron density  $N_0(r = 1.0 R_\odot)$  and scale height  $\lambda_N$  were computed for each leg, as well as the temperature gradient  $\nabla_r T_m$ , and the height-averaged (along the leg) electron temperature  $\langle T_m \rangle$ . As the DENT technique



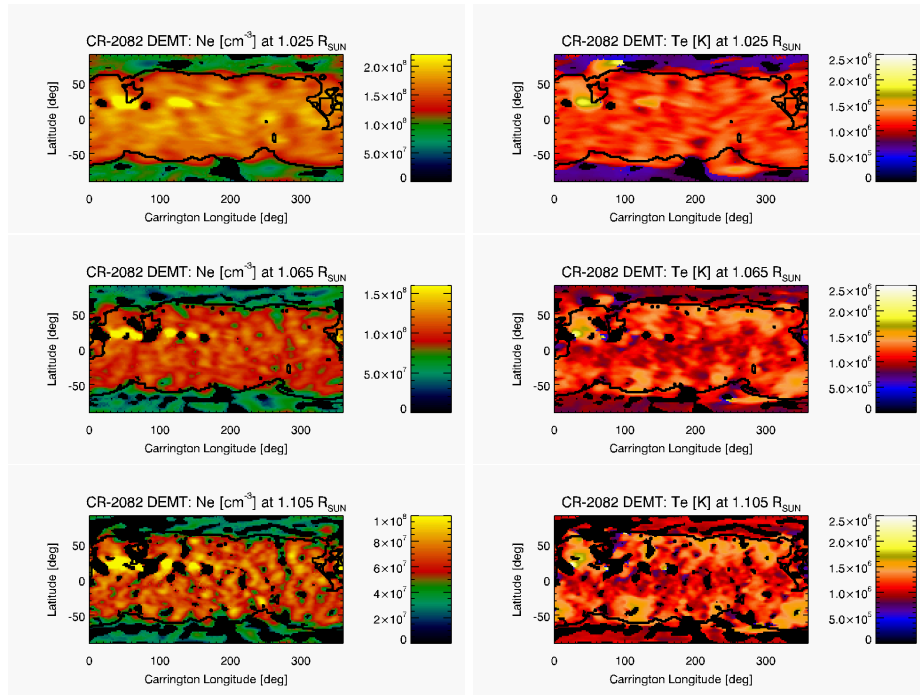


**Figure 1.** Carrington maps of DEMT products  $\sqrt{N_m^2}$  (left panels) and  $T_m$  (right panels) for CR-2082. Top, middle and bottom panels show the results at three heliocentric heights, 1.025, 1.065 and 1.105  $R_\odot$  respectively. Black voxels correspond to non-reconstructed regions (see text in Section 3.1) and thick-black curves indicate the open/closed boundaries.

studies only coronal conditions, *i.e.* above height  $r \approx 1.025 R_\odot$ , the exponential fit to the electron density data as a function of height may be used to compute the tomographic electron density at the coronal base  $\sqrt{N_m^2}(r = 1.025 R_\odot)$  as in previous articles. In this case, for further comparison analysis with the AWSOM results, we selected the lowest height where the results of the MHD model are reliable, that is 1,055  $R_\odot$ .

Aca una linea que linkea la definicion del tipo de lineas en la seccion anterior con las regiones que se ven en la figura que se describe a continuacion

As a way of knowing the physical position of the types of lines defined in Section 2.3, the Figure 3 shows the latitudinal-longitudinal location of the selected lines at 1.105  $R_\odot$  for both rotations. In cyan the type 0 lines are indicated, populating the most equatorial latitudes (dominated mostly by down loops). This kind of structures has been informed in previous works, Lloveras *et al.* (2017) observed down loops in a rotation during the solar minima of 1996 and for the previous rotation CR-2081. A decrease in the amount of down loops in equatorial latitudes could be an indicator of increased coronal activity Nuevo *et al.* (2013). In blue the type I lines, populating all the streamer but mostly the mid latitudes. In red the type II lines, are mostly very large trans-equatorial

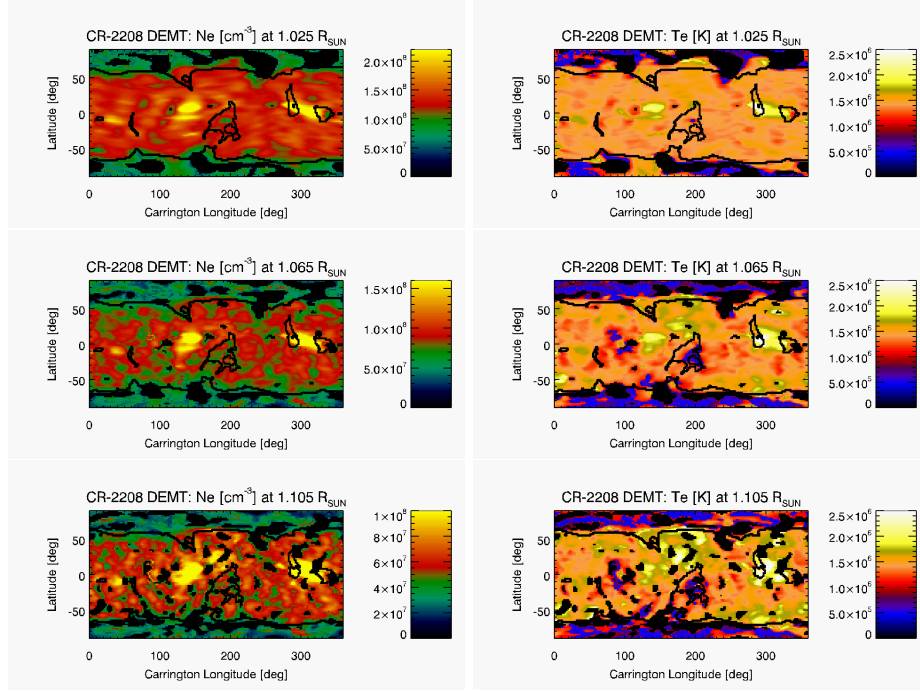


**Figure 2.** Same as Figure 1 but for CR-2208.

field lines forming the envelope of the Streamer belt, and in green dots the type III lines, populating the coronal holes.

Of the 45000 legs selected in 2082, 14% are type 0, 38% are type I, 23% are type II and 25% type III, on the other hand of the 59000 legs selected in 2208, 8% are type 0, 43% are type I, 22% are type II and 30% type III.

This selection of types of lines automatically leads to specific regions arranged along all longitudes associated with different thermodynamic, with good symmetry between both hemispheres in both rotations.

To compare obtained traced results in both rotations and for each type of lines (associated with different types of regions), Figure 4 shows histograms (normalized to the total amount of the field lines selected) of the temperature radial gradients ( $\nabla_r T_m$ ). The lack of population around values close to zero is due to the requirement  $|\rho_t| > 0.5$  which discards quasi-isothermal legs.

Both rotations are characterized by lines of type 0 with mean values of  $-2.5 \text{ MK}/R_\odot$ , mean values of  $2.3 \text{ MK}/R_\odot$  in type I and  $2.4 \text{ MK}/R_\odot$  in type II. The only notable difference is the smaller number of type 0 lines in CR-2208 and the mean value of  $4.5 \text{ MK}/R_\odot$  in type III for CR-2208 which is twice that for the other rotation.

As an example of the traced magnitudes, Figure 5 shows the statistical results of both rotations for all field lines types. From top to bottom type 0 to type III. From left to right the panels show the statistical distribution of  $N_{CB} \equiv \sqrt{N_m^2} (r = 1.055)$ ,  $\lambda_N$ ,  $\langle T_m \rangle$ , in each panel the median  $m$  is indicated.

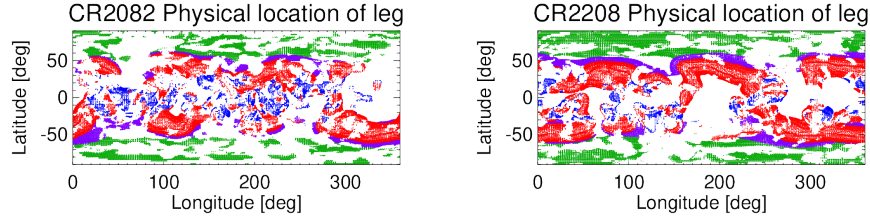


**Figure 3.** Latitude-longitude location of each leg of type 0 (cyan), I (blue), II (red) and III (green) at  $1.105 R_{\odot}$  for CR-2082 (left panel) and CR-2208 (right panel). See Section 2.3 for a definition of the different types of legs. **NOTE: (by ALBERT) The population of DOWN LEGS in CR-2088 is negligible. These are VERY SMALL loops, I am pretty sure but you and Ceci should check it. NOTE: (by ALBERT) This Figure is great, but I do not quite like the choice of colors. I suggest these changes: cyan→blue, blue→red, red→violet. In this way, blue will be DOWN loops and red will be UP loops, as in previous papers. The same change applies to Figure 4. Also, how about making Figures 3 and 4 a single Figure of four panels? Just an idea.**

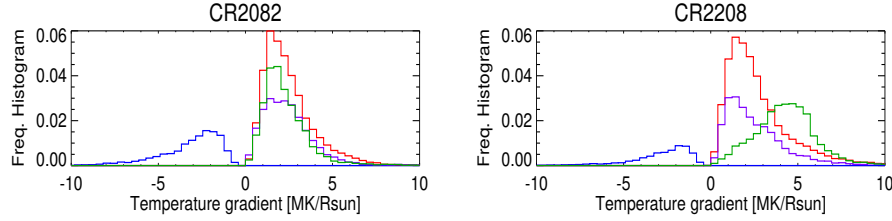


**Figure 4.** Frequency histograms of the temperature radial gradient for the different four types of legs shown in Figure 3 (using the same color code) for CR-2082 (left panel) and CR-2208 (right panel).

For all type of lines, Table 1 summarize the quantitative comparative analysis between the results of the two target rotations sampling both minima. For CR-2082 quantities are expressed as absolute values, while for CR-2208 they are informed relative to the corresponding results for CR-2082. The following major results concerning the structure of each rotation individually and their comparison can be drawn.

si queda una asociacion directa entre los tipos de lineas y las estructuras de streamer, CH etc entonces usaria esos nombres a continuacion.

From the equatorial streamer of both rotations, increasing latitudes show decreasing coronal base density, and increasing density scale height and electron temperature. In both rotations the CH regions are characterized sub-MK temperatures, and coronal base densities of order  $\approx 1/2$  of the equatorial streamer. Histograms with sharp populations indicates that for both rotations the values of all physical quantities exhibit a strong symmetry between both hemispheres.

A comparison of the results between the two rotations shows that CR-2208 is characterized by lower values (between 11% and 16%) of coronal base electron density than CR-2082, higher values of density scale height (between 4% and 19%) and higher values of electron temperature (between 6% and 21%).

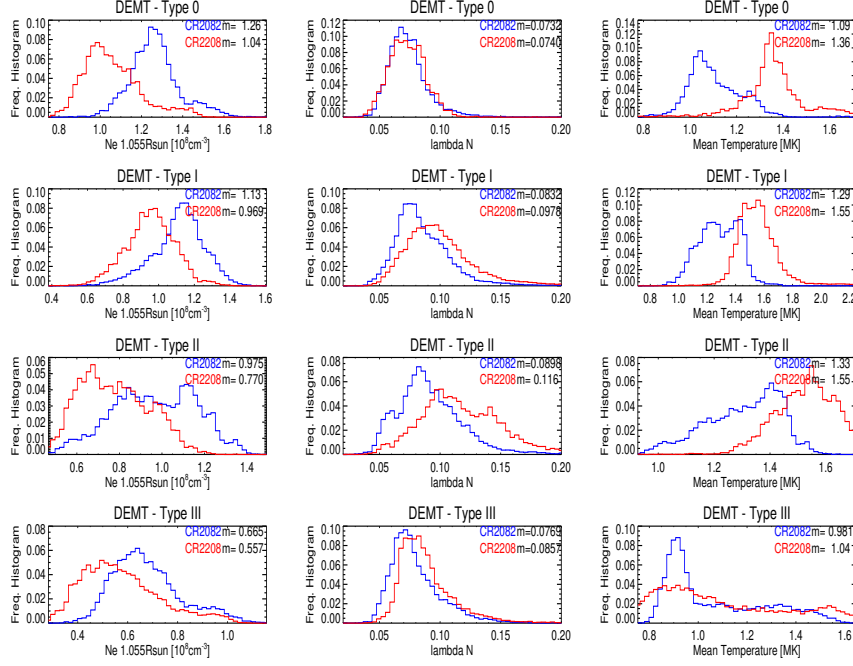


**Figure 5.** Statistical distribution of DGMT results traced along legs of type 0, I, II and III (from top to bottom), as defined in Section 2.3. From left to right: electron density at the coronal base  $N_{CB} \equiv \sqrt{N_m^2}(r = 1.055 R_\odot)$ , electron density scale height  $\lambda_N$ , and loop-averaged electron temperature  $\langle T_m \rangle$ . Results for target rotations CR2082 and CR2208 are shown in blue and red color, respectively. In each panel the median value  $m$  is indicated. **NOTE:** The histogram Figures in this draft need to be improved, in particular font size-and-type need to be optimized for clear reading. Also, we need to improve their X/Y ratio, here I stretched the Y size a bit in the LaTeX source.

### Comienza la energia

**Table 1.** Median value (indicated as “Md”) of the statistical distribution of  $N_{CB}$ ,  $\lambda_N$ , and  $\langle T_m \rangle$  for each coronal type of lines defined in Section 2.3. For CR-2082 values are expressed in absolute terms, while for CR-2208 they are informed as a percentual variation relative to the CR-2082 value.

Type	Md( $N_{CB}$ ) [ $10^8 \text{ cm}^{-3}$ ]	Md( $\lambda_N$ ) [ $10^{-2} R_\odot$ ]	Md( $\langle T_m \rangle$ ) [MK]
0	0.93 (−12.9%)	7.4 (+ 3.9%)	1.11 (+20.7%)
1	0.84 (−11.3%)	8.3 (+15.3%)	1.30 (+16.1%)
2	0.74 (−16.1%)	8.9 (+19.1%)	1.33 (+14.2%)
3	0.48 (−12.5%)	7.7 (+10.5%)	0.98 (+ 5.7%)

To compare integrated quantities along loops, we select those close loops where both legs meet the requirements of Section 2.3. In an analogous way to the legs definition, we will refer to them as loops of type 0, I or II to those whose both legs meeting the criteria. Now the type 0 loops are down loops.

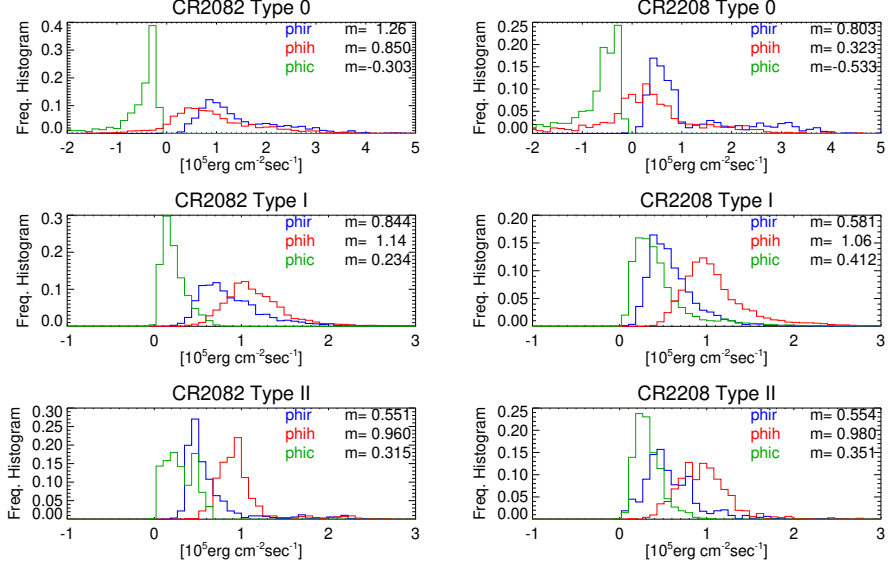


**Figure 6.** Statistical results of the loop integrated energy flux quantities  $\phi_r$ ,  $\phi_c$ , and  $\phi_h$  in colors blue, red and green, respectively for CR-2082 (left) and CR-2208 (right). From top to left loops of type 0, I and II where both legs meets the criteria from Section 2.3. **NOTE:** The type-0 population in CR-22208 is negligible. These are VERY SMALL loops, I am pretty sure but you and Ceci should check it. This can explain the non-physical  $\phi_h < 0$  population. **NOTE:** Utilizar los colores del paper de Cecilia, notar que el conductivo debe ser el verde y el energy input flux (h) debe ser el rojo. De paso, haría el verde un poco menos chillón, como en el paper de Ceci, se verá mejor. En el XYOUTS podés poner la letra griega  $\phi$ , y para que te salga r,c,h como subíndice pero no pequeño usá: “!Dp!N”, donde p=r,c,h.

The frequency histograms of Figure 6 shows the loops-integrated energy quantities:  $\phi_h$ ,  $\phi_r$  and  $\phi_c$  in green, blue, and red lines respectively, for both rotations.

Type 0 loops present slightly larger gradients than type I. Therefore, type 0 present bigger amount, in modulus, of loop-integrated conductive flux. Due conductive flux negative can not be assumed as a loss but it can be contributing to the coronal heating. Thus, to compensate the radiative losses, a lower loop-integrated energy input flux ( $\phi_h$ ) is required.

We can see, on type 0 loops, a median value of energy input flux for CR2082 twice bigger than CR2208. Also, in both rotations, we observe a negative population of loop integrated energy input flux. This can refer to some loops where loop-integrated radiative flux is too small in comparison with the larger gradients of negative conductive flux, resulting in negative energy input flux.

The type I loops show a loop-integrated positive conductive for each loop in both rotations consistent with positive gradients of temperatures. The differences

We found larger temperature gradients for CR2208 than CR2082, but for the most population of loops, the conductive flux have values around  $0.3 \cdot 10^5 [\text{erg sec}^{-1} \text{cm}^{-2}]$  in both rotations. Similar results have been found for loop-integrated radiative flux and energy input flux for both rotations.

No son los mismos colores que el paper de ceci, tmb quizas podriamos poner la cant de LOOPS y los valores medianos, ceci insiste.

### 3.2. Tomography and Models

NOTE: This section will show the results of AWSoM for  $N_e$  and  $T_e$ , and how they compare with the corresponding results of DMT ( $\sqrt{N_m^2}$  and  $T_m$ ). It will first show the Carrington maps of  $N_e$  and  $T_e$  at the same three heights we showed the same maps for the DMT results. Then it will show the lat/lon location of loops of type I, II and III at a middle height, just loke for DMT results. As the two targets are highly axis-symmetric, a first quantitative comparison between AWSoM and DMT will be shown as longitude-averaged latitudinal profiles of the results of both models at a sample height. To make comparisons in distinct magnetic structures, we will also show the average radial dependence of results for loops of type I, II and III, overplotting the AWSoM and the DMT results. For the tree types of loops we will show histograms of the DMT and AWSoM products along field lines. This is a LOT of information from which and we need to pull out a few clear conclussions.

The thermodynamic results of AWSoM are shown in Figures 7 and 8. That is latitude-longitude maps for  $N_e$  and  $T_e$  modeled for CR-2082 and CR-2208 at  $r = 1.025, 1.065$  and  $1.105 R_\odot$ . The black curve denotes the same open-close boundary showed in Figures 1 and 2 respectively.

A visual inspection of these maps shows that both reconstructions are very axysymmetric for  $N_e$  and  $T_e$  as well. The closed region is denser and hotter than the open region. The density and temperature gradients are maximum in the open-close boundary. The open field regions in low latitudes maintain thermodynamic values associated with open regions. CR-2208 shows a well reconstruction of the AR around latitude  $+10^\circ$  and longitude  $300^\circ$  and a slight temperature difference between the poles estoy asumiento que es una AR. In both rotations the open-closed boundaries derived from the AWSoM model match the shape of the contour levels of both the electron density and the electron temperature.

The same intensity scales in both density and temperature can be observed between the tomographic results and those of AWSoM in both rotations, as well as the same thermodynamic structures. That is, equatorial latitudes, mid latitudes and the open regions.

Se presentan los midpoints para awsom que lucen mas rellenos xq no hay down loops y todo es super suave.

In the same way as in Section 3.1, the model results were traced along the magnetic lines obtained with it. This allowed to obtain  $N_e(r)$  and  $T_e(r)$  along the magnetic lines and fit them to the Equations 5 and 6.

The actual version of the AWSoM model can not reproduce down loops, so for a further comparison we only select lines of type I, II and III of those meeting the criteria described in Section 2.3. As a way to understand the distribution

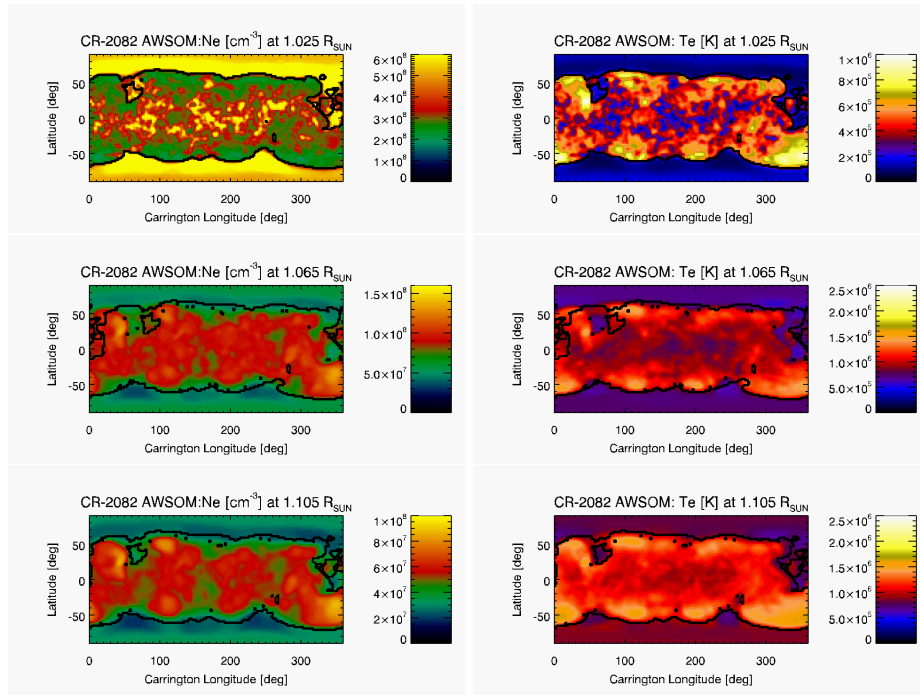


**Figure 7.** Carrington maps of density (left panels) and temperature (right panels) obtained with AWSoM model for the same three heights shown in Figure 1.

of the selected lines, Figure 9 shows the latitudinal-longitudinal location of the selected lines at  $1.105 R_{\odot}$  for both rotations. In blue the type I lines, populating mostly the entire streamer. In red the type II lines, populating the edge that assemble the envelope around the streamer, and in green dots the type III lines, populating the coronal holes.

The reader may notice that these structures are the same as those in Figure 3 but more filled. The cause is twofold, on the one hand the same magnetic model was used to trace both DMT and AWSoM results, on the other hand is because giving the model smoother results, fewer fitted lines are filtered.

To highlight the latitudinal structures observed in Figures 1 and 7 for CR-2082 as well as Figures 2 and 8 for CR-2208, Figure 10 shows for both rotations the latitudinal variation of both the electron density and the electron mean temperature at the height  $r = 1.105 R_{\odot}$ , averaged over all longitudes (excluding the AR). DMT results are shown in blue lines while AWSoM results in red. While the temperature shows a maximum in each hemisphere, the density has a simpler behavior, with higher values in the low-latitudes of the streamer and a nearly monotonic decrease towards larger latitudes. The vertical black lines denotes the average of the open-close boundary in both hemispheres to each rotation.

Me gustaria hacer un comentario de cierre para esta figura que refiera las Figuras 3 y 9, como la linea de abajo, y que conecte con los histogramas que



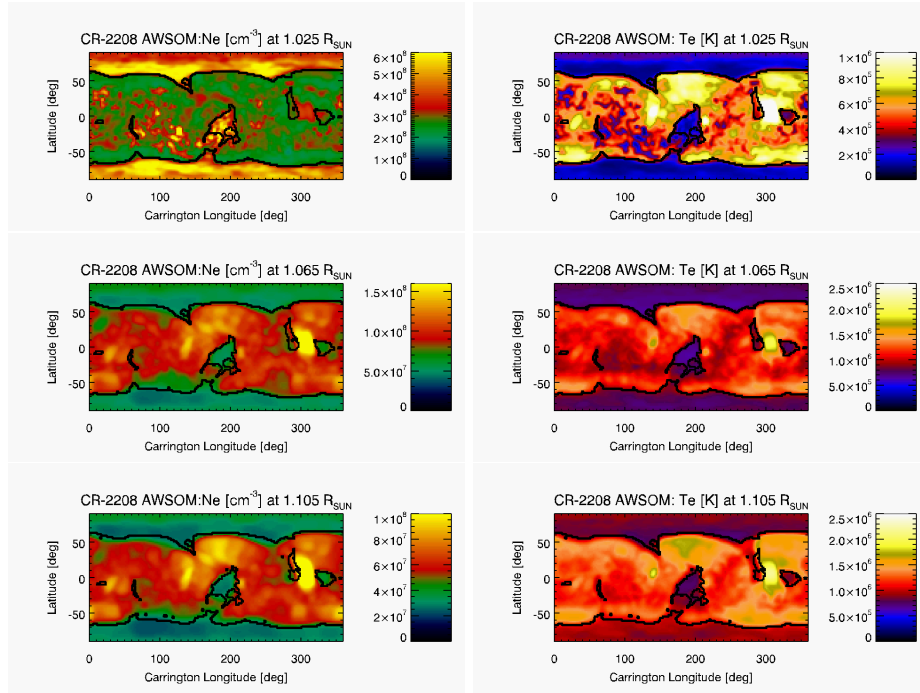


**Figure 8.** Same as Figure 8 for CR-2208.

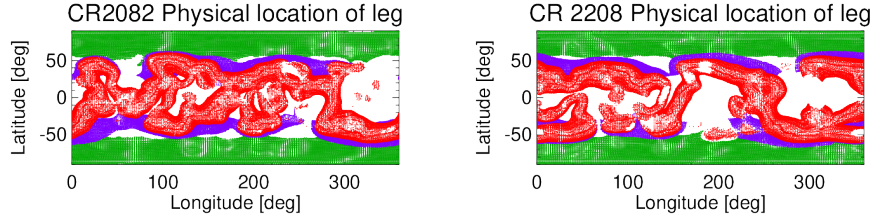


**Figure 9.** Same as Figure 3, but using the density and temperature of the AWSOM model to classify its legs in types I, II and III. The model does not exhibit legs of type 0.

vienen a continuacion. Si no queda bien, hay que mover esta figura entre la actual figura 8 y 9.

This longitude-averaged behaviors match well with the physical locations of the legs shown in Figures 9 and 3.

According to the visual inspection on the maps of carrington, the latitudinal profiles comparing both DGMT and AWSOM results are on the same scale. Little difference in density is observed in CR-2208 and in temperature in CR-2082, while DGMT in CR-2082 was 20% denser. Finally, DGMT results for CR-2208 were 25% hotter in the streamer and 30% colder in the polar zone than AWSOM.



Density profiles on AWSoM show an increase around the polar zone, which seems like an artifact.

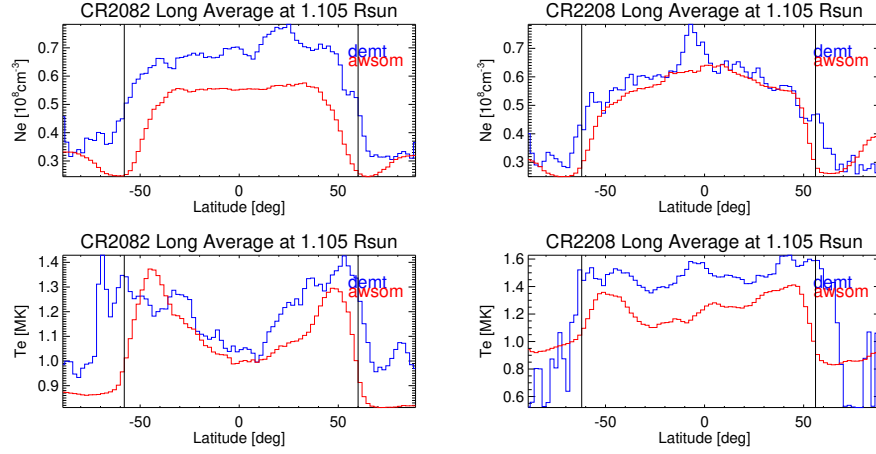


**Figure 10.** Longitude-averaged latitudinal dependence of the electron density (top) and temperature (bottom) for DEMT (blue) and AWSoM (red) results at  $1.105 R_{\odot}$ . The left (right) panels correspond to CR-2082 (CR2208). The vertical black line indicates the longitude-averaged latitudes of the open/close magnetic boundary.

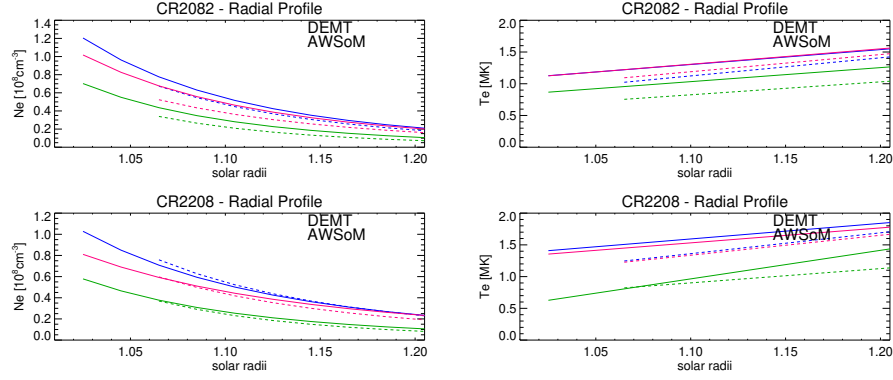
To summarize the comparison between both results during both rotations at full height, it is shown in Figure 11 the average fits of  $N_e(r)$  and  $T_e(r)$  for legs of type I (blue), II (red), and III (green) for both rotations.

In average all temperature and density behavior from both results are on the same scale. The coronal base densities of AWSoM were lower than those of DEMT in CR-2082 and higher in CR-2208. The fact that the density decays to similar values between both results suggests a similar height scale. On the other hand basal temperature of AWSoM was lower in both rotations, but the temperature gradients are very similar in each type of legs, showing a very similar increase of temperature with height.

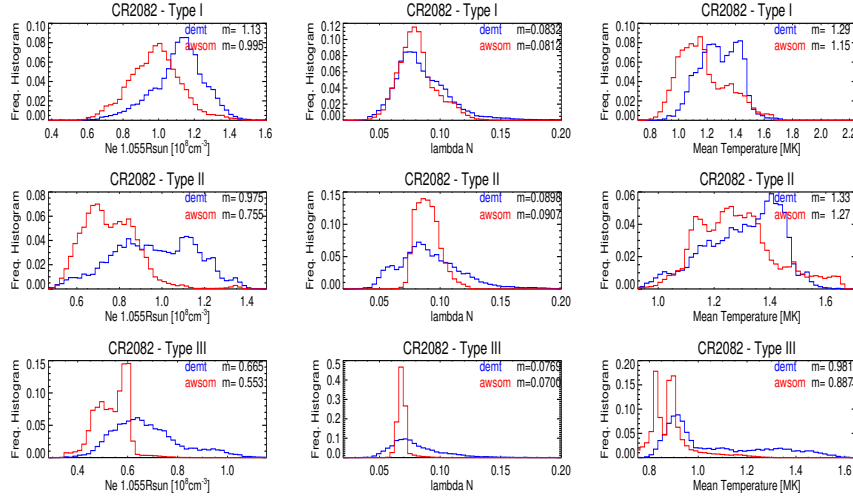
To summarize the statistical comparison, Figure 12 and 13 shows the statistical results of both rotations for the three types of field lines traced with DEMT (blue) and AWSoM results (red). From left to right the panels show the statistical distribution of  $N_{CB}$ ,  $\lambda_N$  and  $\langle T_m \rangle$ . For all types of lines, Table 2 summarizes the median value of the statistical distribution of each physical quantity derived from the analysis. The DEMT quantities are expressed as absolute values, while for AWSoM they are informed relative to the corresponding result for DEMT.

Figure 14 shows the longitude-averaged AWSoM radial wind speed  $V_r$  at  $6 R_{\odot}$ , where all field lines are open. The heliocentric current sheet (HCS) location is indicated by the minimum of the speed curve.

can we say something without having traced the lines? NOTE: (by ALBERT) Todo el punto de la última Figura es precisamente decir algo. La comparación con la Figura 10 muestra una anti-correlación entre la densidad basal de DEMT y la velocidad terminal de AWSoM.



**Figure 11.** Average fits to  $N_e(r)$  (left panels) and  $T_e(r)$  (right panels) for legs of type I (blue), II (red), and III (green), for CR-2082 (top panel) and CR-2208 (bottom panel). Solid lines correspond to DMT results while dashed lines correspond to AWSOM results.



**Figure 12.** Statistical distribution of DMT (blue) and AWSOM (red) results traced along legs of type I, II and III (from top to bottom), as defined in Section 2.3. From left to right: electron density at the coronal base  $N_{CB} \equiv N_e(r = 1.055 R_\odot)$ , electron density scale height  $\lambda_N$ , and leg-averaged electron temperature  $\langle T_m \rangle$ . In each panel the median value  $m$  is indicated.

For each rotation, everything to the south of the HCS maps down to the southern open region in the Figures 10, and the same for the northern hemisphere, showing an anti-correlation between  $N_e$  at low heights and high  $V_r$  at  $6 R_\odot$ .

Voy a intentar jugar con las lineas tipo 3 aumentando su cota inferior de latitud para ver si los histogramas de temp media dejan de ser tan dispersos y se vuelven mas sub-1MK.

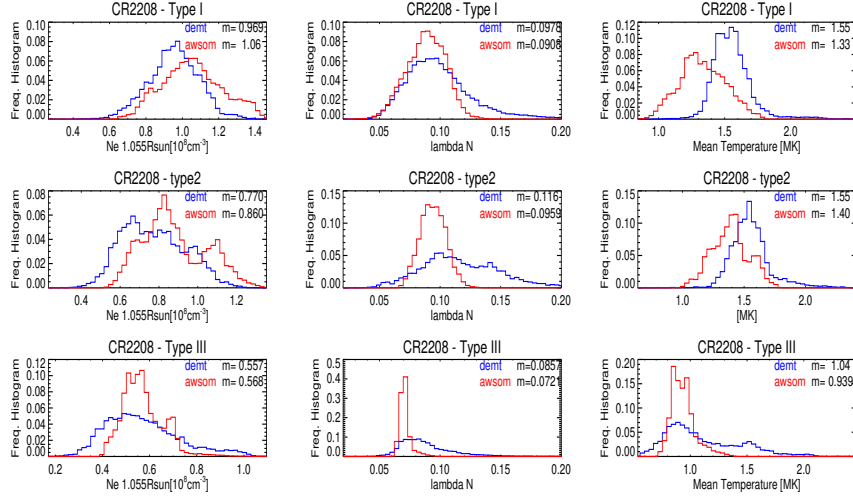


**Figure 13.** Same as Figure 12 for CR-2208.

**Table 2.** Median value (indicated as “Md”) of the statistical distribution of  $N_{CB}$ ,  $\lambda_N$ , and  $\langle T_m \rangle$  for each coronal type of lines defined in Section 2.3. DENT values are expressed in absolute terms, while AWSOM results are informed as a percentual variation relative to the corresponding DENT value.

Type	Md( $N_{CB}$ ) [ $10^8 \text{ cm}^{-3}$ ]	Md( $\lambda_N$ ) [ $10^{-2} R_{\odot}$ ]	Md( $\langle T_m \rangle$ ) [MK]
CR-2082			
1	0.84 (−14.4%)	8.3 (− 2.5%)	1.30 (−10.8%)
2	0.74 (−21.9%)	8.9 (+ 1.0%)	1.33 (− 4.5%)
3	0.82 (−17.9%)	7.7 (− 8.9%)	0.98 (− 9.5%)
CR-2208			
1	0.74 (+ 6.4%)	9.8 (− 7.1%)	1.55 (−12.3%)
2	0.62 (+ 8.2%)	11.6 (−17.2%)	1.55 (− 9.7%)
3	0.42 (− 4.8%)	8.6 (− 8.4%)	1.04 (− 9.7%)

#### 4. Discussion

NOTE: Antes de enviar esto a Michigan se precisa un conjunto de conclusiones compacto y claro. Creo que yo las pondría en tres grupos: a) conclusiones DENT solas (esto incluye estructura termodinámica, up/down loops, energía), b) comparación AWSOM/DENT (la global, es decir promedio longitudinal, y la que diferencia estructuras magnéticas), c) Wind Speed y Densidad basal.

\*Down loops, shift y cranmer comentarios.

\*Energía DENT

We can see, on type 0 loops, a median value of energy input flux for CR2082 twice

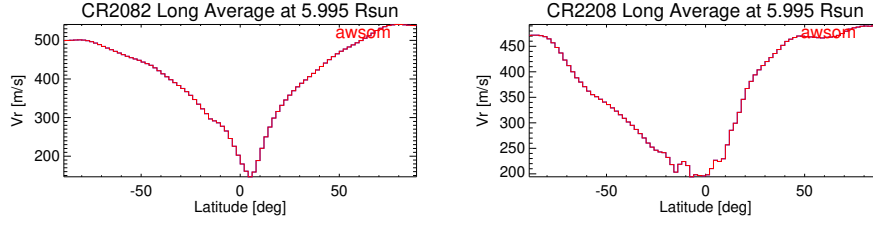


**Figure 14.** Longitude-averaged latitudinal dependence of the AWSoM model wind speed at  $6 R_{\odot}$  for CR2082 (left panel) and CR2208 (right panel).

bigger than CR2208. Also, in both rotations, we observe a negative population of loop integrated energy input flux. This can refer to some loops where loop-integrated radiative flux is too small in comparison with the larger gradients of negative conductive flux, resulting in negative energy input flux.

This effect can be due a subestimation of the density present in the loop or the limited range of temperature used to reconstruct tomographic parameters, that can affect the compute of radiative power. Nevertheless, this population represent lower than the **ALGÚN PORCENTAJE%** of total population in both cases. Bottom panels show the comparison for larger type I loops.

## References

- Aschwanden, M.J.: 2004, *Physics of the Solar Corona. An Introduction*, Praxis Publishing Ltd, ??? ADS.
- Del Zanna, G., Dere, K.P., Young, P.R., Landi, E., Mason, H.E.: 2015, CHIANTI - An atomic database for emission lines. Version 8. *Astron. Astrophys.* **582**, A56. DOI. ADS.
- Frazin, R.A.: 2000, Tomography of the Solar Corona. I. A Robust, Regularized, Positive Estimation Method. *Astrophys. J.* **530**, 1026. DOI. ADS.
- Frazin, R.A., Vázquez, A.M., Kamalabadi, F.: 2009, Quantitative, Three-dimensional Analysis of the Global Corona with Multi-spacecraft Differential Emission Measure Tomography. *Astrophys. J.* **701**, 547. DOI. ADS.
- Lloveras, D.G., Vázquez, A.M., Nuevo, F.A., Frazin, R.A.: 2017, Comparative Study of the Three-Dimensional Thermodynamical Structure of the Inner Corona of Solar Minimum Carrington Rotations 1915 and 2081. *Solar Phys.* **292**(10), 153. DOI. <https://doi.org/10.1007/s11207-017-1179-z>.
- Mac Cormack, C., Vázquez, A.M., López Fuentes, M., Nuevo, F.A., Landi, E., Frazin, R.A.: 2017, Energy Input Flux in the Global Quiet-Sun Corona. *Astrophys. J.* **843**, 70. DOI. ADS.
- Nuevo, F.A., Huang, Z., Frazin, R., Manchester, i. Ward B., Jin, M., Vázquez, A.M.: 2013, Evolution of the Global Temperature Structure of the Solar Corona during the Minimum between Solar Cycles 23 and 24. *Astrophys. J.* **773**(1), 9. DOI. ADS.
- Press, W.H., Teukolsky, S.A., Vetterling, W.T., Flannery, B.P.: 2002, *Numerical recipes in C++ : the art of scientific computing*. ADS.
- Spitzer, L.: 1962, *Physics of Fully Ionized Gases*. ADS.